Materials & Design 252 (2025) 113720

Contents lists available at ScienceDirect

Materials & Design

journal homepage: www.elsevier.com/locate/matdes

Combined X-ray microdiffraction and micromechanical testing for direct measurement of thin film elastic constants

Rebecca Janknecht [a,*], Rainer Hahn [b], Nikola Koutná [a,c], Juraj Todt [d], Michael Meindlhumer [d], Anton Davydok [e], Helmut Riedl [b], Jozef Keckes [c], Paul H. Mayrhofer [a]

[a] Institute of Materials Science and Technology, TU Wien, Austria
[b] Christian Doppler Laboratory for Surface Engineering of High-Performance Components, TU Wien, Austria
[c] Department of Physics, Chemistry, and Biology (IFM), Linköping University, Sweden
[d] Department Materials Science, Montanuniversität Leoben, Austria
[e] Helmholtz-Zentrum Hereon, Institut für Werkstoffphysik, Germany

ARTICLE INFO

Keywords:
Mechanical properties testing
Synchrotron diffraction
Elastic constants
Density Functional Theory (DFT)
Stress and strain

ABSTRACT

Direct measurement of elastic constants for thin films is still far from routine and poses significant technical and analytical challenges compared to bulk materials. Ab initio Density Functional Theory calculations offer theoretical input, however, discrepancies between model systems and real-world properties persist, primarily due to a lack of available experimental data for newly emerging material systems. Moreover, computationally affordable models are typically limited to defect-free single crystals, omitting microstructural effects that strongly influence the material's behavior. This study addresses this gap by proposing a novel experimental approach to measure direction-dependent elastic constants, combining synchrotron microdiffraction and micropillar compression, testing a polycrystalline face-centered cubic $TiN_{0.8}B_{0.2}$ thin film, where linear elastic failure prevails. We have established an advanced in-situ testing environment to continuously record the load–displacement of the indenter while simultaneously collecting the material's deformation response to uniform uniaxial compression. This dynamic approach allows the evaluation of the orientation-dependent elastic strain components and the macroscopic uniaxial compressive stresses, each over time, enabling a differential analysis to assess the elastic and X-ray elastic constants. The excellent agreement between experimental and ab initio data solidifies the here-proposed robust method for direct elastic constant measurements, which is crucial for advancements in thin film material testing.

1. Introduction

While searching for new materials drives progress in materials science, the journey toward their target application requires careful evaluation and testing. In particular, ceramic coatings–fabricated via Physical Vapor Deposition (PVD) methods–have become a central focus of modern materials engineering owing to their superior mechanical properties, e.g., high hardness and wear resistance [1–5]. However, to optimize their performance and ensure reliability under–oftentimes–extreme operating conditions, it is critical to understand their mechanical behavior [6]. Among the commonly analyzed mechanical properties of ceramic thin films such as hardness, H, and fracture toughness, K_{IC}; Young's modulus, E, and Poisson's ratio, ν, serve as fundamental descriptors of a material's response to external forces, where ν quantifies the transverse deformation of a material in response to axial loading and E reflects the material's stiffness in resisting such deformation. In materials engineering, H and K_{IC} are technologically relevant quantities mainly accessible by experimental approaches, where H is usually measured using nanoindentation techniques and K_{IC} can be derived from micromechanical tests (e.g., micro-cantilever bending tests) [7–12].

However, the complex interplay of various contributing factors—including point defects and dislocation dynamics—across multiple length scales makes it difficult to approach these descriptors within the modeling framework. In ceramic coatings, H is not only determined by the ease of the dislocation movement (overcoming the Peierls barrier [13,14]) but also by several hardening mechanisms [15–20] related to the material's microstructure and defect density. Contrarily, theoretical

* Corresponding author.
E-mail address: rebecca.janknecht@tuwien.ac.at (R. Janknecht).

https://doi.org/10.1016/j.matdes.2025.113720
Received 17 July 2024; Received in revised form 6 January 2025; Accepted 11 February 2025
Available online 15 February 2025

hardness and fracture toughness formulas typically take single-crystal elastic constants as the main input [21–23], as these can be quite straightforwardly evaluated by ab initio methods (using the stress–strain [24,25] or the energy-strain method [26]) or machine-learned using suitable ab initio training sets [27–29]. Among the most widely used K_{IC} approximates is Griffith's formula [30], completely omitting plastic deformation [20,31] or any microstructural features that can significantly alter resistance to unstable crack propagation. Griffith's formula relies on the surface energy and the directional Young's modulus, hence, again, elastic constants.

Zero Kelvin ab initio elastic constants calculations, though computationally expensive for chemically complex materials, can nowadays be seen as routine and have been employed to screen across many material systems [32–34]. With the advance of computational power as well as the rapidly developing field of machine-learning interatomic potentials for molecular dynamics, also finite-temperature elastic constants are becoming accessible [35–37]. In a stark contrast, direct elastic constants measurements for ceramic-type coatings are still far from routine. Distinct from bulk materials, their inherent characteristic of being *thin* films introduces additional complexities that necessitate advanced testing methodologies. Additionally, the intrinsic elasto-plastic anisotropy of evolved phases, along with prevalent crystallographic (fiber) textures and distinctive columnar-grained morphologies resulting in poorly understood grain interactions, induces mechanical anisotropy in ceramic thin films. Combined with the intricate properties of the substrate-thin film interface and the size-dependent mechanical properties of crystallites, this makes computational and experimental assessment of the overall mechanical properties very challenging.

Nanoindentation, especially when performed according to Fisher-Cripps [38], provides a convenient approach to determine the reduced polycrystalline modulus of ceramic hard coatings. Using this method, the film-only reduced modulus at zero indentation depth can be extrapolated by fitting a power-law function to the load–displacement data from multiple indentations of varying depths. If the Poisson ratio of the material is known, the polycrystalline Young's modulus can be further calculated. The implementation of X-ray diffraction-based techniques can provide access to the X-ray elastic constants (DECs) of polycrystalline thin films, e.g., by coupling the $\sin^2\psi$ method with the substrate curvature technique [39]. The work of Martinschitz et al. [40] further accounted for the macroscopic elastic anisotropy in textured Cu and CrN thin films by extrapolating the moduli from the experimentally determined thin film DECs. In 2020, Alfreider et al. [41] performed in–situ micro-tensile testing in SEM in combination with a digital image correlation technique to map the true stress–strain state of a nanocrystalline high entropy alloy, enabling the evaluation of the polycrystalline Poisson's ratio. Another method that has been introduced in the last few years is the use of μ-mechanical spectroscopy to determine the elastic modulus of a material by cantilever bending. Examining the shape of the first resonance peak of the indentation setup used, it is possible to detect changes in the damping capability of confined volumes [42,43].

In–situ micromechanical testing methods provide a powerful tool to study material's response to various loading conditions, specifically tailored to investigate small-scale geometries [44]. One such approach combines micromechanical testing and X-ray diffraction, where synchrotron facilities provide advanced access to probe the crystallographic structure and lattice strain of thin films under mechanical stress with exceptional sensitivity [45,46]. Advances in optics and beamline instrumentation allow for intense and highly collimated X-ray beams of very small size–while maintaining high brilliance–that facilitate in-situ measurements of stress–strain distributions in thin films with unprecedented spatial resolution and accuracy, even at the nanoscale [47]. However, it is important to acknowledge that the stress state induced by previously reported in–situ micromechanical testing methods such as nanoindentation or micro-cantilever bending is inherently complex and deviates from the ideally simple uniaxial loading conditions typically assumed in classical mechanics [48–53].

In this study, we present a new methodology designed to accurately measure the direction dependent elastic constants in thin film ceramic hard coatings. Using the combined approach of X-ray microdiffraction and micropillar compression testing, a micropillar fabricated from a 15 μm polycrystalline face centered cubic (fcc) $TiN_{0.8}B_{0.2}$ hard coating (prepared by non-reactive DC PVD sputtering) was tested in uniaxial compression while simultaneously recording its elastic response (to failure) for the {111}, {200}, and {220} crystallographic plane families using a high-energy monochromatic synchrotron radiation source and fast acquisition times (0.55 s). By implementing a high-precision continuous stiffness measurement (CSM) nanoindentation setup, we enabled real-time monitoring of indenter displacement and force during testing. This dynamic approach allowed a differential analysis of the time-dependent elastic deformation of the material under uniform uniaxial loading condition, providing accurate experimental values of elastic and diffraction elastic constants for three independent families of crystallographic planes for a selected face-centered cubic polycrystalline ceramic thin film material. Supported by ab initio density functional calculations, the experimentally determined {*hkl*}-dependent Poisson's ratio, Young's modulus and X-ray elastic constants (DECs) were further compared with their theoretically derived values. By bridging experimental observations with theoretical modeling, we aim to make a step forward in fundamentally understanding mechanical properties of thin film ceramics, using Ti–B–N as a representative material system.

2. Materials and methods

2.1. Thin film deposition

The $TiN_{0.8}B_{0.2}$ coating was deposited on single crystal sapphire $(1\bar{1}02)$ substrates with dimensions of 10 × 10 × 0.53 mm^3 using a modified Leybold Heraeus Z400 deposition system equipped with a 3" unbalanced magnetron sputtering source holding a TiN + TiB_2 + Ti composite target composed of 80 mol.% TiN + 15 mol.% TiB_2 + 5 mol.% Ti with 99.5 % purity from Plansee Composite Materials GmbH. The substrates were ultrasonically pre-cleaned in acetone and isopropyl alcohol for 5 min each, then mounted in the 3'' substrate holder and loaded into the chamber. The target-to-substrate distance was fixed at 40 mm. After reaching the base pressure of $\leq 2{\cdot}10^{-4}$ Pa ($\leq 2{\cdot}10^{-6}$ mbar), the substrates were thermally cleaned at 400 °C for 20 min, followed by Ar ion etching using an Ar pressure (60 sccm Ar flow) of 1.6 Pa and applying a negative bias voltage of −150 V (pulsed DC, 150 kHz, 2496 ns pulse duration). The target was operated at 0.50 A (no substrate bias applied, floating potential −24 V) at an Ar pressure of 0.4 Pa (32 sccm Ar flow) and a substrate temperature of 400 °C for 400 min to achieve a thickness of t ~ 15 μm.

2.2. Thin film characterization

Structural information was obtained by X-ray diffraction (XRD) analysis using a Malvern PANalytical XPert Pro MPD (θ-θ diffractometer) in Bragg-Brentano geometry equipped with a CuK_α radiation source operating at 45 kV and 40 mA monochromatized with a Malvern PANalytical BBHD mirror suppressing K_β. Fracture cross sections were imaged using a Zeiss SIGMA 500 VP Field Emission Gun-Scanning Electron Microscope (FEG-SEM) operating at 10 kV.

Hardness, *H*, and Young's modulus, *E*, were determined by instrumented nanoindentation using a FemtoTools FT-IO4 Femto-Indenter system equipped with a diamond Berkovich tip (calibration was performed on a standard fused silica sample) in Continuous Stiffness Measurement (CSM) mode. 25 load–displacement curves were analyzed according to Oliver and Pharr [54] using a maximum force of 20 mN. The reduced raw moduli data were fitted with a power law as a function of the penetration depth, extrapolated to zero indentation depth, and

corrected according to Fischer-Cripps [38] to yield the film-only Young's modulus.

2.3. Combined synchrotron X-ray microdiffraction and micromechanical testing

A cross-sectional lamella (~100 μm thick in the beam direction) of the $TiN_{0.8}B_{0.2}$ thin film was prepared by cutting and mechanically polishing the coated sapphire substrate. After preparation, the lamella was securely mounted on a sample holder designed for precise alignment in the beam direction without affecting the diffracted beam paths during the experiment. Cylindrical micropillar geometries were fabricated from the cross-sectional lamella by Focused Ion Beam (FIB) milling using a ThermoFisher Scios 2 DualBeam system operated at 30 kV. First, a selected area of the coating material (~120 × 100 × 15 μm^3) was removed with a probe current of 30 nA, except for three free-standing pillars of ~ 10 μm in diameter. By reducing the milling current stepwise to 500 pA, the pillar walls were refined to a final pillar diameter of ~ 5 μm with a height-to-diameter aspect ratio of ~ 3:1 and a taper angle of less than 2°. During the in-situ XRD experiment, one micropillar was compressed using a FemtoTools FT-NMT04 in-situ nanoindentation system operating in intrinsic displacement-controlled mode at a load rate of 5 $nm{\cdot}s^{-1}$, equipped with a FemtoTools FT-S200′000 diamond flat punch tip customized to a final diameter of ~ 10 μm using the FIB system mentioned above. Force and displacement data were collected throughout the experiment, including ~ 100 s after failure. The in-situ micropillar compression testing was conducted at the Nanofocus Endstation of the MiNaXS (P03) beamline at the PETRA III at Deutsches Elektronen-Synchrotron (DESY). The monochromatic X-ray beam with a photon energy of 19.7 keV was focused by a KB mirror setup [47] down to lateral dimensions of 1.5 × 1.5 μm^2. The nanoindentation system was built into the X-ray measurement setup to analyze the micropillar sample in transmission wide-angle diffraction geometry. Before testing, the diamond flat punch tip was centered directly over the pillar top surface to guarantee uniform conditions during loading (see Fig. 1).

In order to center the pillar mid-section to the X-ray beam, the nanoindentation-sample holder assembly was positioned using a hexapod for tilt and rotational alignment, complemented by a linear nanopositioning high load stage for x-, y-, and z-alignment. The diffracted photons were collected using an Eiger X 9 M Hybrid Photon Counting (HPC) 2D detector, with an acquisition time of 0.55 s per frame, positioned at a sample-detector distance of 0.236 m to record the full 111, 200, and 220 Debye-Scherrer rings. The exact parameters of the diffraction geometry were calibrated by measuring a LaB_6 standard reference powder.

2.4. Synchrotron X-ray microdiffraction data analysis

2.4.1. Strain analysis

From the collected Debye-Scherrer ring patterns at the pillar cross-sectional positions (y,z) the orientation-dependent lattice plane spacing $d^{hkl}_{\theta\delta}(y,z)$ can be obtained from its relation to the diffraction vector $\boldsymbol{Q}_{\theta\delta}$ orientation and the diffraction angle $2\theta^{hkl}(\delta)$ magnitude according to Bragg's law (Fig. 1),

$$\lambda = 2d^{hkl}_{\theta\delta}(y,z)\sin\theta^{hkl} \tag{1}$$

whereas λ represents X-ray wavelength.

X-ray elastic strain $\varepsilon^{hkl}_{\theta\delta}(y,z)$ has to be calculated from

$$\varepsilon^{hkl}_{\theta\delta}(y,z) = \frac{d^{hkl}_{\theta\delta}(y,z) - d^{hkl}_0}{d^{hkl}_0} \tag{2}$$

with d^{hkl}_0 as the strain-free lattice plane spacing. Each of the recorded 2D patterns was subjected to azimuthal integration using the open-source software package DPDAK [55], where azimuthal angle δ segments of 10 deg–with δ ranging from −5 to 355°–were integrated. The lattice plane spacing $d^{hkl}_{\theta\delta}(y,z)$ of the {111}, {200}, and {220} peaks was determined by fitting a pseudo-Voigt peak shape function to the 1D intensity profiles–obtained for 36 azimuthal angles δ sections as a function of $2\theta^{hkl}(\delta)$–according to Eq. (1). For each of the three crystallographic plane families, we identified the unstrained lattice plane spacing d^{hkl}_0 from the intersection of the linear fits of the 36 previously calculated $d^{hkl}_{\theta\delta}(y,z)$ data points for 62 shots plotted against $\sin^2\delta$, i.e., 62 collected 2D patterns (up to one recording before failure) were considered for an initial evaluation of the d^{hkl}_0 value (see Supplementary Material). Here, the rationale is that the $d^{hkl}_{\theta\delta}(y,z)$ which has shown to be independent on the applied load must be the strain-free value d^{hkl}_0.

Following the procedure from [51], the measured orientation-dependent elastic strain $\varepsilon^{hkl}_{\theta\delta}(y,z)$ obtained from Eq. (2) can be expressed as a function of six unknown components of the strain tensor, $\varepsilon^{hkl}_{ij}(y,z)$, given by

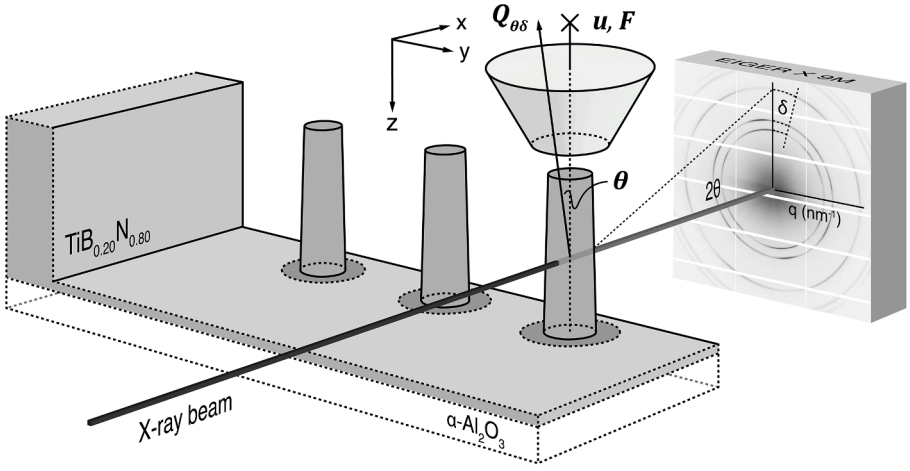

Fig. 1. A schematic view of the in-situ X-ray microdiffraction experiment performed in transmission diffraction geometry using a monochromatic X-ray beam with a spot size of 1.5 × 1.5 μm^2, centered in the mid-section of the free-cut $TiN_{0.8}B_{0.2}$ micropillar sample. The micropillar (aspect ratio 3:1) was loaded in z direction using a diamond flat punch tip with a contact area of ~ 80 μm^2, positioned on top of the pillar along the z axis. The force, $\boldsymbol{F}$, and the indenter displacement, $\boldsymbol{u}$, were simultaneously recorded during testing. 2D diffraction data were collected during the experiment using an Eiger X 9 M photon counting detector. The direction of the strain measurement is identified by the angles θ and δ, where θ is the angle of inclination of the diffraction vector, $\boldsymbol{Q}_{\theta\delta}$, with respect to the equatorial plane defined by the incident beam and δ denotes the azimuth angle within this plane.

$$\varepsilon_{\theta\delta}^{hkl}(y,z) = \sin^2\theta\varepsilon_{xx}^{hkl}(y,z) + \cos^2\theta\sin^2\delta\varepsilon_{yy}^{hkl}(y,z) + \cos^2\theta\cos^2\delta\varepsilon_{zz}^{hkl}(y,z) - \sin2\theta\cos\delta\varepsilon_{zx}^{hkl}(y,z) + \cos^2\theta\sin2\delta\varepsilon_{zy}^{hkl}(y,z) - \sin2\theta\sin\delta\varepsilon_{xy}^{hkl}(y,z) \quad (3)$$

Under uniaxial loading conditions, the pillar experiences compressive strain, $\varepsilon_{zz}^{hkl}(y,z)$, along its longitudinal z-axis. Simultaneously, due to Poisson's effect and its cylindrical geometry, the pillar expands uniformly in all directions perpendicular to the applied load, resulting in equibiaxial strain with, $\varepsilon_{xx}^{hkl}(y,z) = \varepsilon_{yy}^{hkl}(y,z)$, negligible off-axis shear strain, $\varepsilon_{xy}^{hkl}(y,z) = 0$, and equal but near-zero (but not negligible) on-axis shear strain components, $\varepsilon_{zx}^{hkl}(y,z) = \varepsilon_{zy}^{hkl}(y,z) \approx 0$. These simplifications assume an elastic isotropic material behavior, facilitating/reducing the analysis of the pillar deformation from Eq. (3) to three unknown strain components

$$\varepsilon_{\theta\delta}^{hkl}(y,z) = \varepsilon_{yy}^{hkl}(y,z)\left[\sin^2\theta + \cos^2\theta\sin^2\delta\right] + \varepsilon_{zz}^{hkl}(y,z)\cos^2\theta\cos^2\delta - \varepsilon_{zy}^{hkl}(y,z)\left[\sin2\theta\cos\delta - \cos^2\theta\sin2\delta\right] \quad (4)$$

During the experiment, every 5.55 s a 2D diffractogram was recorded over a period of ~ 450 s. From a single Debye-Scherer ring, 36 strain values $\varepsilon_{\theta\delta}^{hkl}(y,z)$ were evaluated according to Eq. (2). For each measurement/shot, we calculated the three unknown strain components $\varepsilon_{yy}^{hkl}(y,z)$, $\varepsilon_{zz}^{hkl}(y,z)$, and $\varepsilon_{zy}^{hkl}(y,z)$ in Eq. (4) by solving the linear equation system (based on 36 linear equations) using a least-squares refinement method. Thus, the orientation-dependent Poisson's ratio, ν^{hkl}, can be extracted from

$$\nu^{hkl} = -\frac{\frac{d}{dt}\varepsilon_{yy}^{hkl}(y,z)}{\frac{d}{dt}\varepsilon_{zz}^{hkl}(y,z)} \quad (5)$$

2.4.2. Poisson's ratio and unstrained lattice parameter refinement

From uniform unidirectional loading conditions, the Poisson's ratio $\nu_{d_0}^{hkl}(y,z)$ of an elastic material is related to the ratio of the transverse and axial strain components, $\varepsilon_{yy}^{hkl}(y,z)$ and $\varepsilon_{zz}^{hkl}(y,z)$, similar to Eq. (5)

$$\nu_{d_0}^{hkl}(y,z) = -\frac{\varepsilon_{yy}^{hkl}(y,z)}{\varepsilon_{zz}^{hkl}(y,z)} \quad (6)$$

where $\nu_{d_0}^{hkl}(y,z)$ can be calculated for each $\varepsilon_{yy}^{hkl}(y,z)$ and $\varepsilon_{zz}^{hkl}(y,z)$ value extracted from the periodic 2D diffraction patterns collected during the compression test. In particular, when ν^{hkl} is obtained from the ratio of the slope between the calculated $\varepsilon_{yy}^{hkl}(y,z)$ and $\varepsilon_{zz}^{hkl}(y,z)$ data points (according to Eqs. (2), (4), and (5)), ν^{hkl} is presumed to be independent of the precise determination of d_0^{hkl} from the $d_{\theta\delta}^{hkl}(y,z)$ vs. $\sin^2\delta$ relation. Notably, the slope-over-time approach is only valid if the rate of deformation is constant (as provided by our indentation setup). Using MATLAB's "fminsearch" optimization algorithm [56] for data points between 67 and 333 s we iteratively adjusted d_0^{hkl} in Eq. (4) to align the d_0^{hkl}-dependent $\nu_{d_0}^{hkl}(y,z)$ values from Eq. (6) by the method of least-squares to closely match the Poisson's ratio from Eq. (5), resulting in a more precise unstrained lattice plane spacing, $d_{0,r}^{hkl}$, for each of the three reflections. Thus, only refined $d_{0,r}^{hkl}$ were used for subsequent calculations including the evaluation of $\varepsilon_{ij}^{hkl}(y,z)$, $\sigma_{zz}^{hkl}(y,z)$, and from there ν^{hkl}, E^{hkl}, $\frac{1}{2}s_2^{hkl}$, and s_1^{hkl}.

2.4.3. Stress analysis

Based on the continuously recorded load–displacement data from the indenter probe, the indentation stress, $\sigma_I(y,z)$, is calculated as the ratio between the applied force $\boldsymbol{F}$ and the area of the pillar mid-section, $A_m(y,z)$

$$\sigma_I(y,z) = -\frac{\boldsymbol{F}}{A_m(y,z)} \quad (7)$$

Notably, the cross-sectional area of the pillar mid-section irradiated during loading is used instead of the top surface contact area, to account for the pillar's taper.

Considering the basic principle of Hooke's law, which connects the induced elastic strain to the applied mechanical stress,

$$\varepsilon_{ij} = S_{ijkl}\cdot\sigma_{kl} \quad (8)$$

where ε_{ij} is the strain tensor, S_{ijkl} is the compliance tensor and σ_{kl} is the stress tensor.

Introducing the {*hkl*}-dependent (X-ray) elastic constants (DECs) [57],

$$s_1^{hkl} = -\frac{\nu^{hkl}}{E^{hkl}} \quad (9)$$

and

$$\frac{1}{2}s_2^{hkl} = \frac{1+\nu^{hkl}}{E^{hkl}} \quad (10)$$

where the proportionally constants E^{hkl} and ν^{hkl} are the Young's modulus and the Poisson ratio, respectively. The uniaxial stress–strain relation is given by

$$\varepsilon_{\theta\delta}^{hkl}(y,z) = s_1^{hkl}\sigma_{zz}(y,z) + \frac{1}{2}s_2^{hkl}\cos^2\theta\cos^2\delta\,\sigma_{zz}(y,z) \quad (11)$$

The linear relationship between the measured strain, $\varepsilon_{\theta\delta}^{hkl}(y,z)$, and the only non-zero deviatoric stress component $\sigma_{zz}(y,z)$– acting under uniaxial compression testing in z-direction–can be expressed according to Eq. (9–11) as

$$\varepsilon_{\theta\delta}^{hkl}(y,z) = \sigma_{zz}^{hkl}(y,z)\left(-\frac{1+\nu^{hkl}}{E^{hkl}}\sin^2\delta\cos^2\theta - \frac{1+\nu^{hkl}}{E^{hkl}}\sin^2\theta + \frac{1}{E^{hkl}}\right) \quad (12)$$

Given the relatively small elastic anisotropy of the $TiN_{0.8}B_{0.2}$ coating material with an ab initio calculated Zener anisotropy ratio of 0.7873 [58] and assuming a uniaxial stress state within the irradiated pillar mid-section during the experiment [59], we can derive the out-of-plane stress, $\sigma_{zz}(y,z)$, for each of the three {*hkl*} reflections following [60]

$$\frac{\partial d_{\theta\delta}^{hkl}(y,z)}{\partial\sin^2\delta} = -\sigma_{zz}(y,z)\frac{1}{2}s_2^{hkl}d_{0,r}^{hkl}\cos^2\theta \quad (13)$$

Using the expression of $\varepsilon_{\theta\delta}^{hkl}(y,z)$ from the normalized lattice plane spacing difference, $d_{\theta\delta}^{hkl}(y,z) - d_{0,r}^{hkl}$, from Eq. (2) and plotting $d_{\theta\delta}^{hkl}(y,z)$ against $\sin^2\delta$, the deviatoric stress, $\sigma_{zz}^{hkl}(y,z)$, can be determined from the slope of the curve, where $\frac{1}{2}s_2^{111} = 2.9879{*}10^{-3}\,\mathrm{GPa}^{-1}$, $\frac{1}{2}s_2^{200} = 2.6400{*}10^{-3}\,\mathrm{GPa}^{-1}$, and $\frac{1}{2}s_2^{220} = 2.9010{*}10^{-3}\,\mathrm{GPa}^{-1}$, and, in addition, the values for s_1^{hkl} are obtained using the ISODEC software package [61] based on the inverse Kröner model [62,63], considering the values from the ab initio calculated stiffness tensor for our deposited Ti–B–N material system with $C_{11} = 548.29$, $C_{12} = 133.15$, and $C_{44} = 163.43$ (cubic symmetry).

2.4.4. Elastic modulus and diffraction elastic constants

Theoretically, the obtained deviatoric stresses, $\sigma_{zz}(y,z)$, remain consistent across different crystallographic planes and correspond to the {*hkl*}-independent macro stresses, $\sigma_I(y,z)$, derived from the probe-to-sample response continuously recorded by the nanoindentation system during loading and calculated according to Eq. (7). By incorporating the discrete indentation stress values, $\overline{\sigma_I}(y,z)$, into Eq. (13), we accessed $\frac{1}{2}S_2^{hkl}$ directly from the experimental data:

$$\frac{\partial d_{\theta\delta}^{hkl}(y,z)}{\partial \sin^2\delta} = -\overline{\sigma_I}(y,z)\left(\frac{1}{2}S_2^{hkl}\right)d_{0,r}^{hkl}\cos^2\theta \tag{14}$$

To synchronize the continuous $\sigma_I(y,z)$ values with the discrete strain, $\varepsilon_{\theta\delta}^{hkl}(y,z)$, and lattice parameter, $d_{\theta\delta}^{hkl}(y,z)$, data (recorded for 5.00 s adding 0.55 s acquisition time), we averaged the indenter stresses, $\overline{\sigma_I}(y,z)$, over 5.55 s time intervals. Combining Eq. (11) and (14) S_1^{hkl} can be derived similarly to $\frac{1}{2}S_2^{hkl}$. Notably, $\frac{1}{2}S_2^{hkl}$ (and S_1^{hkl}) denote the experimentally determined thin film diffraction elastic constants, where $\frac{1}{2}s_2^{hkl}$ (and s_1^{hkl}) refer to the single-crystal DECs derived from C_{ijkl}. Alternatively, $\frac{1}{2}S_2^{hkl}$ can be replaced in Eq. (14) using Eq. (10) and previously calculated ν^{hkl} to further determine the {*hkl*}-dependent Young's modulus, E^{hkl}. To ensure the applicability of Eq. (14) we simplified $\cos^2\theta\left|d_{\theta\delta}^{hkl}(y,z)\right| \approx \cos^2\theta\left|d_{0,r}^{hkl}\right|$.

Additional information can be gathered by plotting the evaluated experimental and ab initio DFT simulated DECs against the parameter 3Γ [64], which is defined as follows

$$3\Gamma = 3\frac{h^2k^2 + k^2l^2 + l^2h^2}{\left(h^2 + k^2 + l^2\right)^2} \tag{15}$$

where *h*, *k*, and *l* are the Millers indices and 3Γ is a single parameter expression for the Miller indices in cubic crystal structures. Plotting the X-ray elastic constants obtained from the single-crystalline ab initio DFT data using the Reuss [57,65], Voigt [66] and Eshelby/Kröner [67] grain interaction models against the 3Γ parameter will lead to 3 lines with different slopes and a single intersection. The calculation of DECs from the single-crystalline stiffness tensor according to the three models was taken from literature and is presented in detail in [68]. Since the theoretical boundaries of possible X-ray elastic constants are set by (i) the Reuss and the Voigt grain-interaction models and (ii) at the intersection these culminate into a single point. In following it will be assumed, that this specific 3Γ value determined for the ab initio DFT data is also valid for the experimentally determined DECs, which will be interpolated to retrieve the experimental polycrystalline {*hkl*}-independent Young's modulus, *E*, and Poisson's ratio, ν.

2.5. Density functional theory calculations

The Vienna Ab-initio Simulation Package (VASP) [69,70] implementation of the Density Functional Theory (DFT) was used to carry out ab initio calculations. The Perdew-Burke-Ernzerhof generalized gradient approximation (GGA) [71] and the plane-wave projector augmented wave (PAW) pseudopotentials [72] were employed. Consistently with our previous study [6], the plane-wave cutoff energy was set to 600 eV, and the reciprocal space was sampled with Γ-centred k-point meshes with a length parameter of 60 Å. All supercells were based on the cubic rocksalt ($Fm\bar{3}m$) TiN structure in which the desired number of B atoms was distributed on the N sublattice (to model the TiB_xN_{1-x} solid solution) using the Special Quasirandom Structure approach [73]. Three supercell orientations were considered: (i) x ∥ [100], y ∥ [010], z ∥ [001] (total of 64 atoms); (ii) x ∥ [110], y ∥ [1$\bar{1}$0], z ∥ [001] (total of 72 atoms); and (iii) x ∥ [111], y ∥ [1$\bar{1}$0], z ∥ [11$\bar{2}$] (total of 72 atoms). The supercells (ii) and (iii), with different numbers of atoms, are visualized in Fig. 1 of [74]. All supercells were fully optimized by relaxing their volume, cell shape, and atomic positions.

The fourth-order elasticity tensor, $\mathbb{C}$, was evaluated for the supercell (i) using the stress–strain approach [24,25] with a strain magnitude of 1.9 %. Applying Voigt's formalism, the tensor was mapped onto a 6 × 6 matrix, C_{ij}, and subsequently projected onto that of a cubic crystal [75], yielding three independent elastic constants: C_{11}, C_{12}, and C_{44}. The polycrystalline Young's modulus, *E*, bulk modulus *B*, and shear modulus *G*, were calculated as Hill's average [76] of the upper bounds according to Reuss's approach (subscript "R") [65] and the lower Voigt's bounds (subscript "V") [66]. The polycrystalline Poisson ratio was calculated using:

$$\nu = \frac{3B - 2G}{6B + 2G} \tag{16}$$

The directional Young's modulus, E^{hkl}, was evaluated following formulas in Nye [77] (p. 143–145). Additionally, we used supercells (ii) and (iii) to simulate uniaxial [111], [001], and [110] compression tests with a 1 % strain step, where at each consecutive step the supercell and the ionic positions were allowed to relax in the directions orthogonal to the applied strain. The predicted lattice parameter changes along the main crystallographic directions allowed us to directly evaluate the (directional) Poisson ratio by calculating the negative first derivative of the resulting average orthogonal strain over the applied strain.

3. Results and Discussion

3.1. Materials characterization

To provide a suitable base coating for in-situ micropillar compression testing, we deposited a 15 μm thick polycrystalline $TiN_{0.8}B_{0.2}$ coating from a TiN + TiB_2 + Ti composite target similar to the 3 μm version characterized by elastic recoil detection analysis (ERDA) reported in [6]. The XRD pattern, Fig. 2a, reveals three distinctive peaks corresponding to the crystallographic planes (111), (200), and (220) of fcc-TiN. The peak shift towards lower 2θ values is mainly due to the incorporation of B into the fcc TiN lattice, as described in detail in previous studies [6]. We further evaluated the residual compressive stresses in Ti–B–N films on the order of about 2.5 GPa, accounting for ~ 1 % of the observed peak shift. Importantly, only the fcc-Ti(N,B) structure is identified, confirming the absence of any other crystalline phase.

The cross section of the $TiN_{0.8}B_{0.2}$ coating in Fig. 2b exhibits a compact, dense growth morphology different from the columnar structure commonly observed in polycrystalline hard coatings. Instead, a refined microstructure is present with an average grain size of 18 ± 7 nm as determined by transmission electron microscopy in [6], where we

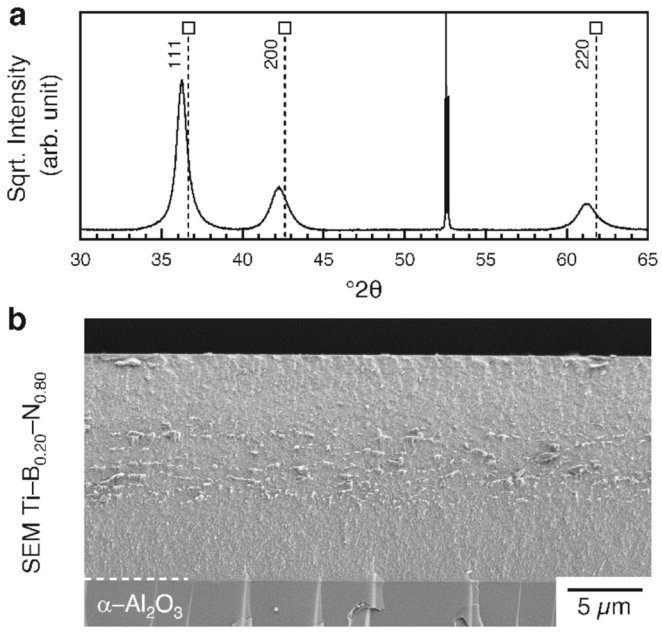

Fig. 2. (a) XRD pattern recorded for $TiN_{0.8}B_{0.2}$ showing standard peak positions corresponding to the (111), $2\theta = 36.663°$, (200), $2\theta = 42.597°$, and (220), $2\theta = 61.814°$ crystallographic planes of fcc-TiN (JCPDS No. 00–038–1420) [78]. (b) Cross section morphology of the deposited $TiN_{0.8}B_{0.2}$ coating with 15 μm film thickness on α-Al_2O_3 substrate.

have recently addressed the effect of B-solubility on the microstructure and mechanical properties of Ti–B–N thin films, which guided our material selection for this experiment.

Micropillars were FIB-milled from the deposited $TiN_{0.8}B_{0.2}$ thin film for subsequent compression testing. Fig. 3a shows the micropillar before testing, with its geometric specifications outlined in white. Our FIB milling protocol induces a nearly symmetrical taper (α_t, left side 1.94°, right side 1.81°) along the pillar, resulting in a slightly non-uniform cylinder with an aspect ratio $h_P : d_T \approx 3$, proven to be practical and suitable for compression testing [59]. Notably, the selected sample geometry should provide a sufficient probe volume (i.e., number of grains) to interact with the X-ray beam ($A_{beam} = 1.5 \times 1.5\,\mu m^2$) in order to facilitate a comprehensive characterization of the material response to applied loads (see Fig. 3a). In [59], Cornec and Lilleodon critically discussed the aspects of determining stress–strain curves from micropillar compression tests. Their computational models verified that a nearly uniaxial stress state occurs in the center of the micropillar over h_M, see Fig. 3a. However, frictional forces and constrained deformation along the top (and bottom) surface of the micropillar result in lateral and shear stresses (i.e., non-uniform stress distributions) due to contact with the indenter during loading. We therefore chose to irradiate the specimen at its midpoint. Post-testing, the fracture surface of the $TiN_{0.8}B_{0.2}$ micropillar exhibits characteristic features associated with brittle failure. The SEM image in Fig. 3b shows a distinct fracture surface morphology characterized by smooth fracture lines, with the right side of the pillar separated from the remaining left part. This unilateral fracture indicates an abrupt and catastrophic failure event that propagated along the vertical axis of the pillar. The absence of significant plastic deformation features (e.g., distortion or shear bands), further confirms that the fracture mechanism is predominantly brittle.

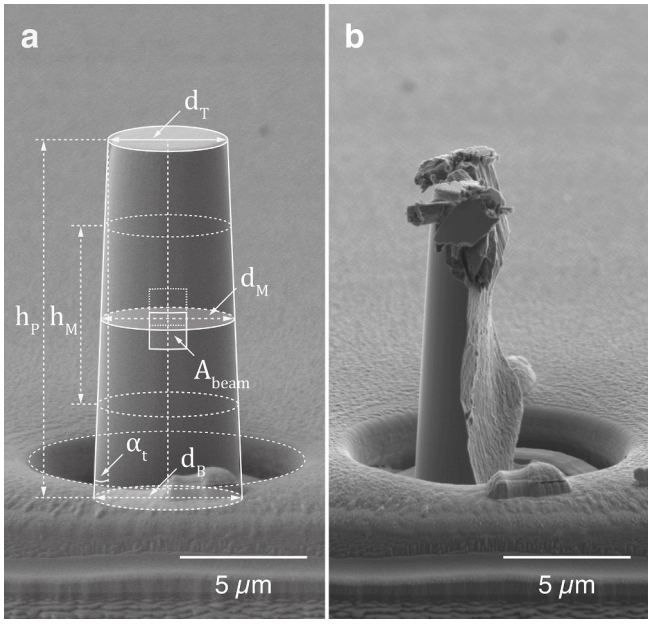

Fig. 3. (a) Schematic representation of the micropillar's geometric parameters. The actual height of the pillar, $h_P = 15.01 \pm 0.05\,\mu m$, aligns with the film thickness with a taper angle $\alpha_t < 2^\circ$. The top surface diameter, d_T, measures $4.57 \pm 0.05\,\mu m$, while the bottom diameter, d_B, is $\approx 5.5\,\mu m$; albeit with a slight circular foot transition that complicates precise determination. The mid-section of the pillar, measured at half its height has a diameter of $d_T = 5.04 \pm 0.05\,\mu m$ with a cross-sectional area $A_m = 19.96\,\mu m^2$. The central region where the micropillar experiences a nearly uniaxial stress state is marked as $h_M = 7.51 \pm 0.05\,\mu m$. During the experiment, the center of the pillar was fixed in transmission geometry perpendicular to the beam direction with a cross-section diameter $A_{beam} = 1.5 \times 1.5\,\mu m^2$. Auxiliary lines were extrapolated to the foot level to illustrate the complete pillar geometry. (b) Fractured $TiN_{0.8}B_{0.2}$ micropillar after compression testing, displaying brittle behavior consistent with the ceramic nature of the material.

3.2. X-ray strain analysis

In-situ compression testing was conducted at a constant loading rate of 5 nm·s^{-1} while recording a 2D diffraction pattern at regular intervals of 5.00 s (adding the acquisition time of the detector of 0.55 s) for a period of 450 s, ensuring controlled loading conditions for precisely monitoring the pillar material's mechanical response throughout the test. All experimental results were plotted for 400 s, with loading starting at ~ 42 s and failure occurring at ~ 350 s.

Fig. 4 presents the three resulting strain components ε_{zz}^{hkl}, ε_{yy}^{hkl}, and ε_{zy}^{hkl} for three crystallographic plane families {*hkl*}, {111}, {200}, and {220}. The strain values were determined by 2D X-ray diffraction data analysis (as detailed in the experimental section) according to Eq. (7). The pre-

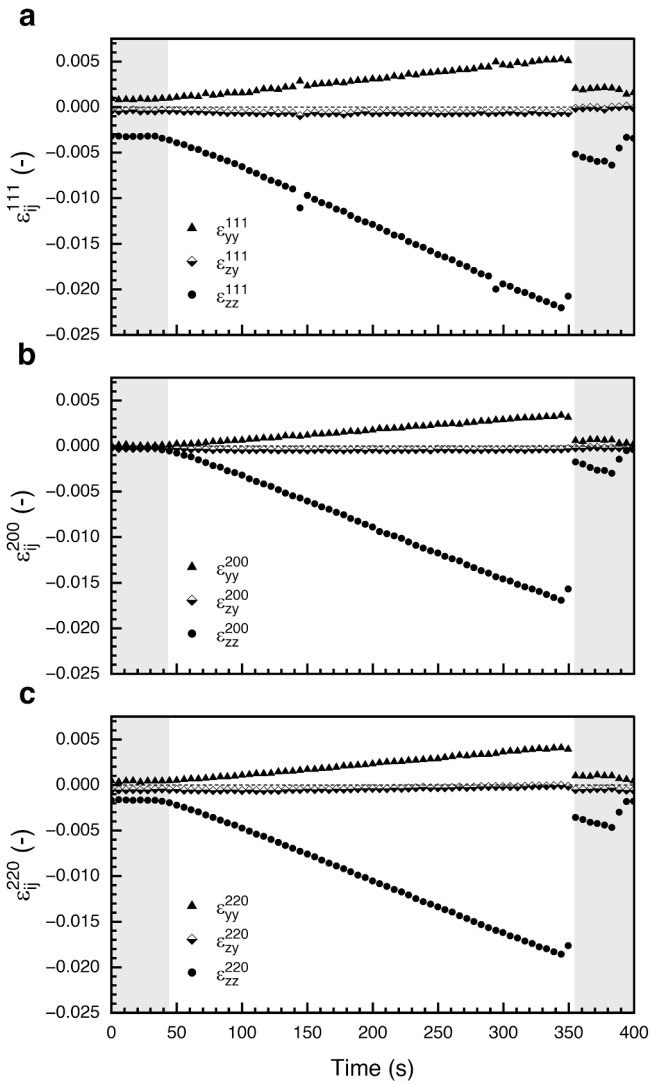

Fig. 4. Elastic strain components of $TiN_{0.8}B_{0.2}$ derived from in-situ uniaxial pillar compression testing for three distinct crystallographic planes {*hkl*} are shown: (a) ε_{ij}^{111}, (b) ε_{ij}^{200}, and (c) ε_{ij}^{220}. Each plot illustrates the calculated strain data points at load time (i) in the loading direction z, ε_{zz}^{hkl} (indicated by filled circles,) (ii) in the lateral direction, $\varepsilon_{yy}^{hkl} = \varepsilon_{xx}^{hkl}$ (filled triangles), and (iii) the shear strain components, $\varepsilon_{zy}^{hkl} = \varepsilon_{zx}^{hkl}$ (shown as half-filled diamonds). The strain values recorded during pre-loading and post-failure of the pillar appear on a grey background.

dominant axial strain component, ε_{zz}^{hkl}, corresponds to the loading direction, i.e., the out-of-plane direction of the pillar, reflecting the compression of the pillar along its z-axis due to the applied load until failure at ~ 2 % strain; an expected value for ceramic hard coating materials [50]. Conversely, the Poisson effect implies lateral expansion in the x and y directions to accommodate the volume change resulting from the pillar compression in the z direction. Under uniform uniaxial loading conditions, the lateral strain components for a cylindrical pillar are equal in magnitude ($\varepsilon_{yy}^{hkl} = \varepsilon_{xx}^{hkl}$, i.e., $\varepsilon_{xy}^{hkl} = \varepsilon_{yx}^{hkl} = 0$ is valid) and represent the elastic deformation perpendicular to the direction of loading. Although the shear strain components ($\varepsilon_{zy}^{hkl} = \varepsilon_{zx}^{hkl}$) are expected be close to zero, the minimal shear deformations observed do not indicate significant deviation from uniform loading conditions or inelastic material behavior during the experiment.

The almost linear progression of ε_{yy}^{hkl} and ε_{zz}^{hkl} over the time of applied load suggests a predominantly linear elastic material behavior that is relatively consistent across the three crystallographic planes (Fig. 4a-c). However, we observe a nuanced elastic anisotropy in the material's response to uniaxial compression. Specifically, ε_{yy}^{111} and ε_{zz}^{111} propagated to slightly higher magnitudes compared to the in-plane and out-of-plane strain components recorded for the {220} and {200} plane families (compare Fig. 3a-c). Note that in sputtered polycrystalline thin films, the presence of crystallographic textures can contribute to the macroscopic anisotropy of the material [40]. The presence of (virtual) residual strains, particularly notable in the z direction for the {111} peak, ε_{zz}^{111}, may also partly stem from lattice defects favoring specific crystallographic plane families. However, using free-standing pillar geometries for in–situ mechanical testing offer advantages over previously reported methods [44,79] in revealing the intrinsic coating material's mechanical properties by allowing the material to deform freely under applied load. Free-cutting a cylindrical shaped pillar out of the deposited coating material mitigates residual stresses–commonly observed in conventional sputtered PVD thin films–providing a uniform stress–strain distribution throughout the specimen and reducing frictional forces during deformation [59]. In combination with synchrotron X-ray microdiffraction this approach allowed us to collect in–situ the detailed information on the pillar's deformation response to uniaxial compression in the lateral and longitudinal direction for three independent crystallographic plane families {111}, {200}, and {220}. The so-obtained elastic strain components ε_{ij}^{hkl} are essential for accessing the {*hkl*}-dependent elastic constants.

The Poisson's ratio for each crystallographic plane families {111}, {200}, and {220}, as shown in Fig. 5, was determined from the negative ratio of the slope between the transverse strain components, ε_{yy}^{hkl}, and the slope of the axial strain components, ε_{zz}^{hkl}, over a period of 61–327 s. Eq. (5). The ν^{hkl} values obtained for $\nu^{111} = 0.241$, $\nu^{200} = 0.199$, and $\nu^{220} = 0.222$ are in the range of 0.2–0.3 commonly observed for ceramic hard coatings and suggest a moderate level of anisotropy in the coating's elastic response. Although {*hkl*}-dependent Poisson's ratios for Ti–B–N coatings have not been studied so far, the values obtained from our experiment appear reasonable when compared to those reported for fcc-TiN thin films [80–82]. Complementarily, the {*hkl*}-dependent Poisson's ratios for $TiN_{0.8}B_{0.2}$ were calculated based on Eq. (6), where the negative ratio for each transverse and axial strain data point recorded over the time to failure was derived. However, the resulting 64 $\nu_{d_0}^{hkl}$ values for each crystallographic plane significantly deviated from the one ν^{hkl} value derived from Eq. (5), as clearly shown in Fig. 5a–c. To refine the determination of $\nu_{d_0}^{hkl}$, we iteratively adjusted the strain-free lattice parameter, $d_0^{hkl} \rightarrow d_{0,r}^{hkl}$, to fit the $\nu_{d_0}^{hkl}$ values to ν^{hkl} by the method of least-squares, as detailed in the experimental part. The refined values are denoted as $d_{0,r}^{hkl}$ and $\nu_{d_0}^{hkl}$.

Accurate determination of d_0^{hkl} is critical in diffraction-based stress–strain analyses, often presenting the primary source of uncertainty [83,84]. Even minor alterations in d_0^{hkl} significantly impact the calculated parameters. In this study, the uncertainties of $\nu_{d_0}^{hkl}$ associated with d_0^{hkl}(see Fig. 4a–c) were < 0.1 % underpinning the meticulous precision required in X-ray strain analysis. Ideally, adjusting d_0^{hkl} does not affect the slope of the strain data points (Fig. 3a-c), since the calculation of ν^{hkl} (expressed as in (Eq. (8)), remains invariant to variations in d_0^{hkl}. This independence arises from the fundamental nature of Poisson's ratio, a material constant that defines the material's transverse response under axial loading. Despite many other factors (i.e., instrumental limitations, sample preparation, or local changes in microstructure and chemical composition) that can complicate the experimental determination of d_0^{hkl}, optimizing d_0^{hkl} to ensure consistency between the calculated $\nu_{d_0}^{hkl} \rightarrow \nu_{d_{0,r}}^{hkl}$ values obtained from Eq. (6) and ν^{hkl} appears to be a valid approach for $d_{0,r}^{hkl}$-refinement and to enhance the precision of our results.

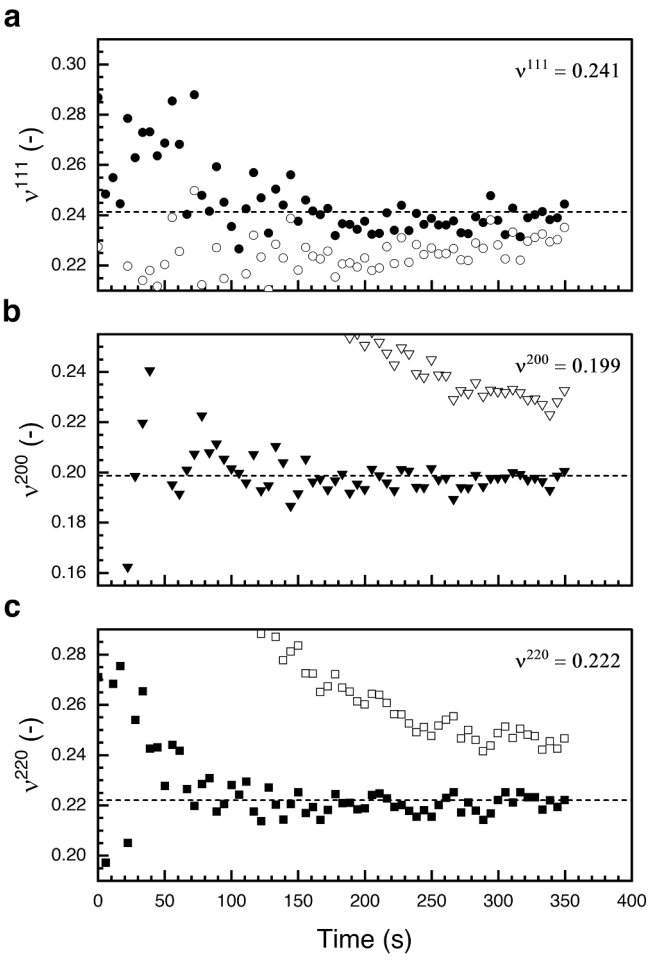

Fig. 5. Poisson's ratio values of $TiN_{0.8}B_{0.2}$ obtained for three crystallographic plane families {111}, {200}, and {220} shown in panels (a) circular symbols, (b) triangular symbols, and (c) square symbols, respectively. The dashed horizontal line in each panel represents the ν^{hkl} value calculated from the negative ratio of the slope of the lateral and axial strain components, as indicated in the upper right corner. All framed symbols denote the initial $\nu_{d_0}^{hkl}$ values calculated pointwise from the negative ratio of ε_{yy}^{hkl} and ε_{zz}^{hkl}, while filled symbols show the least squares fitted $\nu_{d_{0,r}}^{hkl}$ values after iterative "fminsearch" (a derivative-free minimization routine of MATLAB) optimization of the strain-free lattice parameter from d_0^{hkl} to $d_{0,r}^{hkl}$. Notably, certain initial $\nu_{d_0}^{hkl}$ values deviate strongly from the ν^{hkl} target value and appear (not visible) outside the plot.

3.3. X-ray uniaxial stress analysis

Besides investigating elastic properties elastic properties of the $TiN_{0.2}B_{0.8}$ coating, we further analyzed the deviatoric stress components of the micropillar under uniaxial compression loading along the z-direction. This required the use of Eq. (13), which facilitate the calculation of σ_{zz} based on the pre-determined strain components, ε_{ij}^{hkl}, as described in the Methodology section.

Our results in Fig. 6 show that the calculated stresses for $\sigma_{zz}\{200\}$ and $\sigma_{zz}\{220\}$ closely match the indenter stress, σ_I, all in GPa. The deviation of $\sigma_{zz}\{111\}$ from an initial ~ zero stress state presumably prone to texture effects in {111} plane of the material system. Of particular interest, however, is the observed linear increase in compressive stress in the loading direction up to failure. The slope of the three deviatoric stresses, closely aligns with the macroscopic indenter stresses, suggesting a coherent loading response of the {*hkl*} crystallographic plane families inside the probing volume of the pillar. This observation is consistent with the assumption of uniform uniaxial loading conditions and suggests a linear elastic response in the micropillar during testing. Despite the shifted values for {111} lattice plane families observed in the pre-loading state, as we are interested in how well our calculated $\frac{1}{2}s_2^{hkl}$ and s_1^{hkl} values match with the macroscopic stresses,σ_I, only the coherency of the slopes is relevant. The micropillar failure at 7.5 GPa (according to σ_I) adds credibility to the validation of the experiment and is in good agreement with fracture behavior observed in other ceramic hard coatings under similar compressive loading scenarios [50].

Since the compressive load is applied uniformly along the z axis, the resulting stress state is assumed to be homogeneously distributed in the mid-section of the pillar according to [59]. Therefore, the deviatoric stress components, σ_{zz}, in our experiment are expected–and shown–to be equal in slope compared to the macroscopic (i.e., {*hkl*}-independent) stress response derived from the indenter, σ_I, allowing the experimental determination of $\frac{1}{2}S_2^{hkl}$ by differentiating Eq. (14). In detail, we plotted $\frac{\partial d_{\theta\delta}^{hkl}}{\partial \sin^2\delta}$ over $\overline{\sigma_I}$ and calculated $\frac{1}{2}S_2^{hkl}$ from the first derivative of the linear fit. The polycrystalline directional-dependent X-ray elastic constants link the macro stresses, σ_I, with the directional-dependent strains, ε_{ij}^{hkl}, caused by them. Therefore, $\frac{1}{2}S_2^{hkl}$ and S_1^{hkl} can be inferred from the measured direction-dependent strain changes and the simultaneously recorded macroscopic stresses generated by compressing the pillar with a constant loading rate. The recording of data on the elastic behavior of a material over time allows for the calculation of elastic and diffraction (X-ray) elastic constants from the slope of underlying equations mentioned in the methodology section. This differential approach offers a more precise determination than discrete measurements, as previously demonstrated in the calculation of the Poisson ratio. Given that Eq. (11) is in the form of $y = k{\cdot}x + d$, where S_1^{hkl} is included in the in the y-intercept term, we plotted $\varepsilon_{\theta\delta}^{hkl}(y,z)$ $\text{atsin}^2\delta = 0$ against $\overline{\sigma_I}(y,z)$. The elimination of the $k \bullet x$ term allows for the linear fitting of the data points and to calculate S_1^{hkl} from the slope of the line (similar to the procedure for $\frac{1}{2}S_2^{hkl}$). Subsequently, E^{hkl} values were calculated using the fundamental relationship between elastic and X-ray elastic constants (Eqs. (4) and (5)).

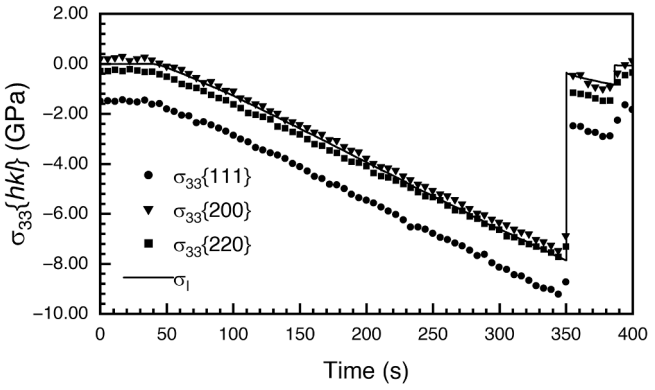

Fig. 6. Uniaxial compressive stress analysis of a $TiN_{0.8}B_{0.2}$ micropillar showing the stress components evaluated for {111} (circular symbols), {200} (triangular symbols), and {220} (square symbols) evaluated for the three crystallographic planes along with the continuous stress measurements from the indenter, σ_I (continuous line). The plot illustrates stress evolution over load time to failure at 350 s and −7.86 GPa.

3.4. Thin film elastic constants

Following the experimental determination of the direction dependent thin film elastic constants, ν^{hkl} and E^{hkl}, as well as the X-ray elastic constants $\frac{1}{2}S_2^{hkl}$ and S_1^{hkl}, our investigation extends to the derivation of the polycrystalline thin film elastic constants, ν and E. To interpolate the polycrystalline values from the single crystal X-ray elastic constants, we utilized the known coefficients from the stiffness tensor (C_{11} = 548.29, C_{12} = 133.15, and C_{44} = 163.43) for fcc-$TiN_{0.94}B_{0.06}$ to calculate $\frac{1}{2}s_2^{hkl}$ and s_1^{hkl} according to each of the three models proposed by Voigt, Reuss, and Eshelby/Kröner, as described in detail in [62,65–67,83]. Please note, that we used the stiffness tensor for a fcc-$TiN_{0.94}B_{0.06}$ crystal to account for the insufficient B incorporation in our deposited $TiN_{0.8}B_{0.2}$ coating. The peak shift observed in the XRD pattern in Fig. 2a indicates that ca. 3 at% B is incorporated in the fcc-TiN lattice with the surplus of B segregated amorphously at the grain boundaries [6]—only the crystals contribute to the analysis.

The calculated single-crystal X-ray elastic constants can be represented by the orientation parameter, 3Γ, which expresses the three Miller indices *h*, *k*, and *l* as a single parameter and ranges from 0 to 1, where 3Γ{200} = 0, 3Γ{220} = 0.75, and 3Γ{111} = 1. Specifically for cubic material systems, the Reuss and Eshelby/Kröner models show a linear distribution of $\frac{1}{2}s_2^{hkl}$ and s_1^{hkl} over the parameter 3Γ, whereas Voigt grain interaction model yields a single set of DECs that are independent of the {*hkl*}-plane families (Please note, that generally the Voigt model assumes all grains are strained identically). The intersection between the three models in Fig. 7 indicates where the {*hkl*}-dependent DECs, $\frac{1}{2}s_2^{hkl}$ and s_1^{hkl}, are assumed to be similar to the {*hkl*}-independent (macroscopic) quasi-isotropic polycrystalline thin film elastic constants, i.e., Young's modulus, *E*, and Poisson's ratio, ν. By interpolating the experimentally determined polycrystalline thin film X-ray elastic constants S_1^{hkl} (Fig. 7a) and $\frac{1}{2}S_2^{hkl}$ (Fig. 7b) to 3Γ = 0.54–obtained from the intersection of the ab initio DFT data–we can determine *E* = 443GPa and ν = 0.213 according to Eqs. (9) and (10).

The comparison in Fig. 7ab indicates a strong agreement between experimentally determined thin film X-ray elastic constants, S_1^{hkl} and $\frac{1}{2}S_2^{hkl}$, and theoretical predictions, particularly for the Eshelby/Kröner model. Notably, the slopes of the linear fits match closely, especially for $\frac{1}{2}S_2^{hkl}$ and $\frac{1}{2}s_2^{hkl}$. This confirms previous findings indicating the improved performance of the Eshelby/Kröner model in predicting the mechanical elastic behavior of quasi-isotropic polycrystals [83] and that these parameters can be used for stress analysis. We further observe that the s_1^{hkl} values derived from the ISODEC software based on the inverse Kröner model follow those of Eshelby/Kröner. However, in the case of $\frac{1}{2}s_2^{hkl}$, the latter is in better agreement with the experimentally determined $\frac{1}{2}S_2^{hkl}$ values (compare Fig. 7a and 7b). The ab initio DFT data for $\frac{1}{2}s_2^{hkl}$ shows a slightly better agreement with the experimental data compared to s_1^{hkl}. This discrepancy suggests potential opportunities for refinement in the simulation methodologies, particularly in relation to Poisson's contraction, which will be the focus of future research.

Finally, summarized in Table 1, we present the results of our in–situ experimental approach to determine the {*hkl*}-dependent as well as the polycrystalline thin film elastic and X-ray elastic constants for $TiN_{0.8}B_{0.2}$

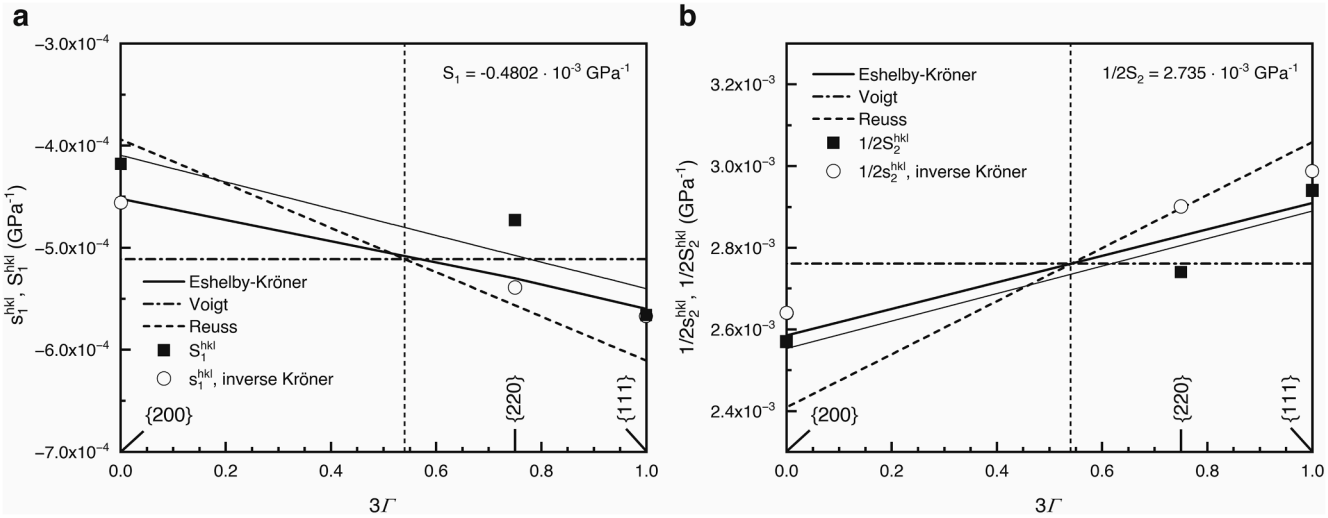

Fig. 7. 3Γ plot of the single crystal diffraction elastic constants, (a) s_1^{hkl} and (b) $\frac{1}{2}s_2^{hkl}$, derived from the models of Voigt (dashed-dotted line), Reuss (dashed-line), and Eshelby/Kröner (solid line) using the ab into calculated coefficients of the stiffness tensor C_{11}, C_{12}, and C_{44} for fcc-$TiN_{0.94}B_{0.06}$. The experimentally determined X-ray elastic constants (squared symbols) for {111}, {200}, and {220} are predicted to be linear over 3Γ. The hypothetical 3Γ value (0.54) of the unknown quasi-isotropic polycrystalline thin film elastic constants is estimated to be similar to the calculated single crystal X-ray elastic constants (marked by the vertical small-dashed line). The circular symbols represent s_1^{hkl} and $\frac{1}{2}s_2^{hkl}$ calculated from ISODEC software (based on the inverse Kröner model) and used for the deviatoric stress analysis.

Table 1
Summary of the experimental values for the {*hkl*}-dependent and macroscopic thin film elastic constants ν^{hkl}, ν, E^{hkl}, E, and the X-ray elastic constants $\frac{1}{2}S_2^{hkl}$ and S_1^{hkl} for $TiN_{0.8}B_{0.2}$ compared to the theoretically derived {*hkl*}-dependent and macroscopic single–crystal elastic and X-ray elastic constants, $\frac{1}{2}s_2^{hkl}$ and s_1^{hkl} (derived from the inverse Kröner model) for fcc-$TiN_{0.94}B_{0.06}$. $\frac{1}{2}S_2$ and S_1 correspond to {*hkl*}-independent experimental thin film X-ray elastic constants interpolated from the intersection of the $3\Gamma^{hkl}$ plot in Fig. 7ab, where $\frac{1}{2}s_2$ and s_1 are the theoretical {*hkl*}-independent single–crystal X-ray elastic constants from the Reuss model at the intersection.

Experimentally determined elastic and X-ray elastic constants for $TiN_{0.8}B_{0.2}$ thin films					
{*hkl*}	{111}	{200}	{220}	macroscopic	
ν^{hkl}(−)	0.241 ± 0.004	0.199 ± 0.001	0.222 ± 0.001	ν(−)	0.213
E^{hkl}(GPa)	422 ± 2	467 ± 2	446 ± 2	E(GPa)	443
$\frac{1}{2}S_2^{hkl}$(10^{-3} GPa^{-1})	2.94 ± 0.01	2.57 ± 0.01	2.74 ± 0.01	$\frac{1}{2}S_2$(10^{-3} GPa^{-1})	2.74
S_1^{hkl}(10^{-3} GPa^{-1})	−0.57 ± 0.06	−0.42 ± 0.02	−0.47 ± 0.02	S_1(10^{-3} GPa^{-1})	−0.48
Ab inito calculated elastic and X-ray elastic constants for single-crystal fcc-$TiN_{0.94}B_{0.06}$					
{*hkl*}	{111}	{200}	{220}	macroscopic	
ν^{hkl}(−)	0.255	0.189	0.240	ν(−)	0.229
E^{hkl}(GPa)	408	496	427	E(GPa)	442
$\frac{1}{2}s_2^{hkl}$(10^{-3} GPa^{-1})	2.9879	2.6400	2.9010	$\frac{1}{2}s_2$(10^{-3} GPa^{-1})	2.76
s_1^{hkl}(10^{-3} GPa^{-1})	−0.5669	−0.4556	−0.5390	s_1(10^{-3} GPa^{-1})	−0.51

compared to the theoretically predicted single crystal values. Where possible, the standard error was calculated using Gaussian error propagation. The polycrystalline Young's modulus, E_I, was additionally extrapolated from nanoindentation measurements of the coating with $E_I = 454 \pm 33$ GPa (not added to the table) and matches the polycrystalline thin film Young's modulus interpolated from the in-situ pillar compression experiment ($E = 443$ GPa) as well as the value obtained from the DFT calculations based on the Hill grain interaction model ($E = 442$ GPa), as described in detail in the methodology section.

The residual stresses of the $TiN_{0.8}B_{0.2}$ coating, measured at 0.6 GPa, are relatively low compared to E_I. Therefore, the E_I value can be considered a valid benchmark for comparison with the other experimental and theoretical results. The measured hardness, $H = 32.1 \pm 1.9$ GPa, also falls within the expected range of 35 GPa, in agreement with our previous experimental results [6,85]. The values are slightly higher than those reported for pure TiN in the literature [80–82], indicating a greater compliance for $TiN_{0.8}B_{0.2}$ compared to TiN. As previously explained, increasing the B content in fcc-TiN results in a reduction of E [6]. This decrease in E can be attributed to the increase in lattice spacing, leading to severe lattice distortions. Furthermore, adding B introduces lattice defects such as N-vacancies or amorphous B-rich grain boundary phases. These irregularities disrupt the uniformity of the fcc-TiN lattice and consequently alter the material's stiffness.

4. Summary and Conclusion

In this study, we aim to develop a new in-situ test routine to experimentally determine the direction dependent elastic constant of polycrystalline thin films using in-situ micro-pillar compression testing coupled with X-ray strain analysis. To provide a suitable quasi-isotropic ceramic coating for testing, we deposited a 15 μm $TiN_{0.8}B_{0.2}$ thin film ($H = 32.1 \pm 1.9$ GPa, $E_I = 454 \pm 33$ GPa), characterized by a dense, small-grained (non-columnar) microstructural cross section. X-ray diffraction analysis confirmed the presence of a single-phase crystalline fcc-TiN structure with peak shifts attributed to 3 at% B incorporation within the fcc-TiN lattice, while excess B is segregated as amorphous B-rich grain boundary phases. The micro-pillar (aspect ratio 3:1) fabricated by a conventional FIB milling process displayed a symmetric taper ($\alpha < 2°$) and was qualified for controlled compression testing. By implementing an advanced in-situ nanoindentation setup, we subjected the $TiN_{0.8}B_{0.2}$-micropillar to uniform uniaxial compression with a constant deformation rate until failure, while simultaneously performing transmission X-ray microdiffraction to detect the {*hkl*}-dependent deformation response for the {111}, {200}, and {220} plane families. The experiment directly obtained the direction-dependent Poisson ratio, ν^{hkl}, from the negative ratio of the slopes of the linear elastic strain response, $\frac{d}{dt}\epsilon_{ij}^{hkl}$, to the

applied load over time in the transverse and axial directions until the pillar failed with absence of plastic deformation. Additionally, the determination of the strain-free lattice spacing, $d_0^{hkl} \rightarrow d_{0,r}^{hkl}$, was refined by iteratively adjusting the $\nu_{d_0}^{hkl}$ values obtained from the negative strain ratio $-\frac{\epsilon_{yy}^{hkl}}{\epsilon_{zz}^{hkl}}$ to fit the differentially derived Poisson ratio ν^{hkl}. Considering this deviation, we were able to refine d_0^{hkl} with the required accuracy of 10^{-5} nm for X-ray diffraction stress–strain analysis. This experimental refinement procedure provides a d_0^{hkl}-accuracy three magnitudes higher than DFT. The unique capability of the experiment to simultaneously record deformation changes, $\frac{\partial d_{\phi\delta}^{hkl}}{\partial \sin^2\delta}$, and corresponding uniaxial macroscopic stresses, $\overline{\sigma_I}$, allowed to determine the thin film X-ray elastic constants, $\frac{1}{2}S_2^{hkl}$, S_1^{hkl}, followed by the direction-dependent thin film Young's modulus E^{hkl}. The thereby derived elastic constants such as $\nu^{111} = 0.241 \pm 0.004$, $\nu^{200} = 0.199 \pm 0.001$, $\nu^{220} = 0.222 \pm 0.001$, $E^{111} = 422 \pm 2$ GPa, $E^{200} = 467 \pm 2$ GPa, and $E^{220} = 446 \pm 2$ GPa, excellently agree with DFT-values of $\nu^{111} = 0.255$, $\nu^{200} = 0.189$, $\nu^{220} = 0.240$, $E^{111} = 408$ GPa, $E^{001} = 496$ GPa, and $E^{101} = 427$ GPa.

Having successfully calculated the directional-dependent thin film elastic constants and X-ray elastic constants from our experiments we interpolated the polycrystalline (macroscopic) thin film elastic constants, ν and E, from the calculated single-crystal X-ray elastic constants, $\frac{1}{2}s_2^{hkl}$, s_1^{hkl}, using the theoretical models proposed by Reuss, Voigt, and Eshelby/Kröner. Particularly, the Eshelby/Kröner model showed the best alignment with experimental data.

CRediT authorship contribution statement

Rebecca Janknecht: Writing – original draft, Visualization, Methodology, Investigation, Conceptualization. **Rainer Hahn:** Writing – review & editing, Supervision, Methodology, Investigation, Conceptualization. **Nikola Koutná:** Writing – review & editing, Formal analysis. **Juraj Todt:** Writing – review & editing, Validation, Conceptualization. **Michael Meindlhumer:** Writing – review & editing, Validation, Conceptualization. **Anton Davydok:** Resources, Investigation. **Helmut Riedl:** Writing – review & editing, Funding acquisition. **Jozef Keckes:** Writing – review & editing, Validation. **Paul H. Mayrhofer:** Writing – review & editing, Supervision, Project administration, Funding acquisition, Conceptualization.

Declaration of competing interest

The authors declare that they have no known competing financial interests or personal relationships that could have appeared to influence the work reported in this paper.

Acknowledgements

The authors acknowledge TU Wien Bibliothek for financial support through its Open Access Funding Program. We sincerely thank the X-ray Center (XRC) at TU Wien for beam time. The computational results presented have been achieved using the National Academic Infrastructure for Supercomputing in Sweden (NAISS) at the Linköping University partially funded by the Swedish Research Council through grant agreement no. 2022-06725 and the Vienna Scientific Cluster (VSC) in Austria. The financial support by the Austrian Federal Ministry for Digital and Economic Affairs, the National Foundation for Research, Technology and Development and the Christian Doppler Research Association is gratefully acknowledged (Christian Doppler Laboratory "Surface Engineering of high-performance Components"). We acknowledge DESY (Hamburg, Germany), a member of the Helmholtz Association HGF, for the provision of experimental facilities. Parts of this research were carried out at PETRA III and we would like to thank A. D. for assistance in using beamline P03 MiNaXS. Beamtime was allocated for proposal I20221274 EC. M. M. and J. K. gratefully acknowledge the financial support for this work provided by Österreichische Forschungsförderungsgesellschaft mbH (FFG), project "CuttingEdgeNanoMat" (No. 46568228). Finally, R. J. and R. H. would like to express their gratitude to Grégory Abadias for his valuable comments provided during the 93rd IUVSTA workshop 2023 in Seggau.

Appendix A. Supplementary data

Supplementary data to this article can be found online at https://doi.org/10.1016/j.matdes.2025.113720.

Data availability

Data will be made available on request.

References

[1] P.H. Mayrhofer, H. Clemens, F.D. Fischer, Materials science-based guidelines to develop robust hard thin film materials, Prog. Mater. Sci. 146 (2024) 101323.
[2] M. Stueber, H. Holleck, H. Leiste, K. Seemann, S. Ulrich, C. Ziebert, Concepts for the design of advanced nanoscale PVD multilayer protective thin films, J. Alloys. Compd. 483 (2009) 321–333.
[3] H. Kindlund, D.G. Sangiovanni, I. Petrov, J.E. Greene, L. Hultman, A review of the intrinsic ductility and toughness of hard transition-metal nitride alloy thin films, Thin Solid Films 688 (2019).
[4] W. Zhai, L. Bai, R. Zhou, X. Fan, G. Kang, Y. Liu, K. Zhou, Recent progress on wear-resistant materials: designs, properties, and applications, Adv. Sci. 8 (2021).
[5] B. Breidenstein, B. Denkena, P. Wolters, M. Keitel, W. Tillmann, D. Stangier, N. F. Lopes Dias, A novel development of sustainable cutting inserts based on PVD-coated natural rocks, Mater. Today Sustainability 24 (2023).
[6] R. Janknecht, R. Hahn, N. Koutná, T. Wójcik, E. Ntemou, A. Steiger-Thirsfeld, Z. Chen, A. Kirnbauer, P. Polcik, S. Kolozsvári, Z. Zhang, D. Primetzhofer, P. H. Mayrhofer, A Strategy to Enhance the B-Solubility and Mechanical Properties of Ti–B–N Thin Films, Acta. Mater. 271 (2024) 119858.
[7] C. Fuger, R. Hahn, A. Hirle, P. Kutrowatz, M. Weiss, A. Limbeck, O. Hunold, P. Polcik, H. Riedl, Revisiting the origins of super-hardness in TiB2+z thin films – Impact of growth conditions and anisotropy, Surf. Coat. Technol. 446 (2022).
[8] A. Bahr, S. Richter, R. Hahn, T. Wojcik, M. Podsednik, A. Limbeck, J. Ramm, O. Hunold, S. Kolozsvári, H. Riedl, Oxidation behaviour and mechanical properties of sputter-deposited $TMSi_2$ coatings (TM = Mo, Ta, Nb), J. Alloys. Compd. 931 (2023).
[9] J. Ast, M. Ghidelli, K. Durst, M. Göken, M. Sebastiani, A.M. Korsunsky, A review of experimental approaches to fracture toughness evaluation at the micro-scale, Mater. Des. 173 (2019).
[10] J.H. Choi, H. Kim, J.Y. Kim, K.H. Lim, B.C. Lee, G.D. Sim, Micro-cantilever bending tests for understanding size effect in gradient elasticity, Mater. Des. 214 (2022).
[11] W. Luo, C. Kirchlechner, X. Fang, S. Brinckmann, G. Dehm, F. Stein, Influence of composition and crystal structure on the fracture toughness of NbCo2 Laves phase studied by micro-cantilever bending tests, Mater. Des. 145 (2018) 116–121.
[12] J. Ast, G. Mohanty, Y. Guo, J. Michler, X. Maeder, In situ micromechanical testing of tungsten micro-cantilevers using HR-EBSD for the assessment of deformation evolution, Mater. Des. 117 (2017) 265–266.
[13] P. Peierls, The size of a dislocation, Proc. Phys. Soc. 52 (1940) 34–37.
[14] F.R.N. Nabarro, Dislocations in a simple cubic lattice, Proc. Phys. Soc. 59 (1947) 256–272.
[15] R.L. Fleischer, Substitutional solution hardening, Acta. Metall. 11 (1963) 203–209.
[16] E.O. Hall, The Deformation and Ageing of Mild Steel: III Discussion of Results, Proc. Phys. Soc. London,. Sect. B 64 (1951) 747.
[17] N.J. Petch, The influence of grain boundary carbide and grain size on the cleavage strength and impact transition temperature of steel, Acta. Metall. 34 (1986) 1387–1393.
[18] E. Orowan, Fracture and strength of solids, Prep. Prog. Phys. 12 (1949) 185–232.
[19] J.G. Byrne, M.E. Fine, A. Kelly, Precipitate hardening in an Aluminium-Copper Alloy, Phil. Mag. 6 (1961) 1119–1145.
[20] G.I. Taylor, A theory of the plasticity of crystals, Z Kristallogr – Cryst. Mater. 89 (1934) 375–385.
[21] X.Q. Chen, H. Niu, D. Li, Y. Li, Modeling hardness of polycrystalline materials and bulk metallic glasses, Intermetallics (Barking) 19 (2011) 1275–1281.
[22] E. Mazhnik, A.R. Oganov, A model of hardness and fracture toughness of solids, J. Appl. Phys. 126 (2019).
[23] H. Niu, S. Niu, A.R. Oganov, Simple and accurate model of fracture toughness of solids, J. Appl. Phys. 125 (2019).
[24] Y. Le Page, P. Saxe, Symmetry-general least-squares extraction of elastic data for strained materials from ab initio calculations of stress, Phys. Rev. B. Condens. Matter. Mater. Phys. 65 (2002) 1–14.
[25] R. Yu, J. Zhu, H.Q. Ye, Calculations of single-crystal elastic constants made simple, Comput. Phys. Commun. 181 (2010) 671–675.
[26] Y. Le Page, P. Saxe, Symmetry-general least-squares extraction of elastic coefficients from ab initio total energy calculations, Phys. Rev. B. Condens. Matter. Mater. Phys. 63 (2001).

[27] V. Revi, S. Kasodariya, A. Talapatra, G. Pilania, A. Alankar, Machine learning elastic constants of multi-component alloys, Comput. Mater. Sci. 198 (2021).
[28] G. Vazquez, P. Singh, D. Sauceda, R. Couperthwaite, N. Britt, K. Youssef, D. D. Johnson, R. Arróyave, Efficient machine-learning model for fast assessment of elastic properties of high-entropy alloys, Acta. Mater. 232 (2022).
[29] H. Levämäki, F. Tasnádi, D.G. Sangiovanni, L.J.S. Johnson, R. Armiento, I. A. Abrikosov, Predicting elastic properties of hard-coating alloys using ab-initio and machine learning methods, NPJ. Comput. Mater. 8 (2022).
[30] A.A. Griffith, The phenomena of rupture and flow in solids, Phil. Trans. R. Soc. Lond. A. 221 (1921) 163–198.
[31] G.R. Irwin, Analysis of Stresses and Strains Near the End of a Crack Traversing a Plate, J. Appl. Mec. 12 (1957) 361–364.
[32] V. Moraes, H. Riedl, C. Fuger, P. Polcik, H. Bolvardi, D. Holec, P.H. Mayrhofer, Ab I nitio inspired design of ternary boride thin films, Sci. Rep. 8 (2018).
[33] K. Balasubramanian, S.V. Khare, D. Gall, Valence electron concentration as an indicator for mechanical properties in rocksalt structure nitrides, carbides and carbonitrides, Acta. Mater. 152 (2018) 175–185.
[34] N. Koutná, A. Brenner, D. Holec, P.H. Mayrhofer, High-throughput first-principles search for ceramic superlattices with improved ductility and fracture resistance, Acta. Mater. 206 (2021).
[35] H. Chan, B. Narayanan, M.J. Cherukara, F.G. Sen, K. Sasikumar, S.K. Gray, M.K. Y. Chan, S.K.R.S. Sankaranarayanan, Machine Learning Classical Interatomic Potentials for Molecular Dynamics from First-Principles Training Data, J. Phys. Chem. C 123 (2019) 6941–6957.
[36] F. Tasnádi, F. Bock, J. Tidholm, A.V. Shapeev, I.A. Abrikosov, Efficient prediction of elastic properties of Ti0.5Al0.5N at elevated temperature using machine learning interatomic potential, Thin. Solid. Films 737 (2021).
[37] S. Lin, L. Casillas-Trujillo, F. Tasnádi, L. Hultman, P.H. Mayrhofer, D. G. Sangiovanni, N. Koutná, Machine-learning potentials for nanoscale simulations of tensile deformation and fracture in ceramics, NPJ Comput. Mater. 10 (2024).
[38] A.C. Fischer-Cripps, Critical review of analysis and interpretation of nanoindentation test data, Surf. Coat. Technol. 200 (2006) 4153–4165.
[39] E. Eiper, K.J. Martinschitz, J. Keckes, Combined elastic strain and macroscopic stress characterization in polycrystalline Cu thin films, Powder. Diffr. 21 (2006) 25–29.
[40] K.J. Martinschitz, R. Daniel, C. Mitterer, J. Keckes, Elastic constants of fibre-textured thin films determined by X-ray diffraction, J. Appl. Crystallogr. 42 (2009) 416–428.
[41] M. Alfreider, M. Meindlhumer, V. Maier-Kiener, A. Hohenwarter, D. Kiener, Extracting information from noisy data: strain mapping during dynamic in situ SEM experiments, J. Mater. Res. 36 (2021) 2291–2304.
[42] M. Alfreider, M. Meindlhumer, T. Ziegelwanger, R. Daniel, J. Keckes, D. Kiener, Revealing dynamic-mechanical properties of precipitates in a nanostructured thin film using micromechanical spectroscopy, MRS. Bull. 49 (2024) 49–58.
[43] M. Alfreider, I. Issa, O. Renk, D. Kiener, Probing defect relaxation in ultra-fine grained Ta using micromechanical spectroscopy, Acta. Mater. 185 (2020) 309–319.
[44] M.D. Uchic, D.M. Dimiduk, J.N. Florando, W.D. Nix, Sample dimensions influence strength and crystal plasticity, Science 305 (2004) 986–989.
[45] J. Todt, J. Zalesak, C. Krywka, J. Keckes, Influence of gradient residual stress and tip shape on stress fields inside indented TiN hard coating, Adv. Eng. Mater. 23 (2021).
[46] S. Heinze, T. Krülle, L. Ewenz, C. Krywka, A. Davydok, A. Stark, R. Cremer, C. Leyens, Influence of the deposition process and substrate on microstructure, phase composition, and residual stress state on as-deposited Cr-Al-C coatings, Mater. Des. 225 (2023).
[47] C. Krywka, H. Neubauer, M. Priebe, T. Salditt, J. Keckes, A. Buffet, S.V. Roth, R. Doehrmann, M. Mueller, A two-dimensional waveguide beam for X-ray nanodiffraction, J. Appl. Crystallogr. 45 (2012) 85–92.
[48] G. Lotze, A.H.S. Iyer, O. Bäcke, S. Kalbfleisch, M.H. Colliander, In situ characterization of stresses, deformation and fracture of thin films using transmission X-ray nanodiffraction microscopy, J. Synchrotron. Radiat. 31 (2024) 42–54.
[49] M. Meindlhumer, L.R. Brandt, J. Zalesak, M. Rosenthal, H. Hruby, J. Kopecek, E. Salvati, C. Mitterer, R. Daniel, J. Todt, J. Keckes, A.M. Korsunsky, Evolution of stress fields during crack growth and arrest in a brittle-ductile CrN-Cr clamped-cantilever analysed by X-ray nanodiffraction and modelling, Mater. Des. 198 (2021).
[50] L. Zauner, R. Hahn, E. Aschauer, T. Wojcik, A. Davydok, O. Hunold, P. Polcik, H. Riedl, Assessing the fracture and fatigue resistance of nanostructured thin films, Acta. Mater. 239 (2022).
[51] A. Zeilinger, J. Todt, C. Krywka, M. Müller, W. Ecker, B. Sartory, M. Meindlhumer, M. Stefenelli, R. Daniel, C. Mitterer, J. Keckes, In-situ observation of cross-sectional microstructural changes and stress distributions in fracturing TiN thin film during nanoindentation, Sci. Rep. 6 (2016).
[52] J. Todt, C. Krywka, Z.L. Zhang, P.H. Mayrhofer, J. Keckes, M. Bartosik, Indentation response of a superlattice thin film revealed by in-situ scanning X-ray nanodiffraction, Acta. Mater. 195 (2020) 425–432.
[53] W. Ecker, J. Keckes, M. Krobath, J. Zalesak, R. Daniel, M. Rosenthal, J. Todt, Nanoscale evolution of stress concentrations and crack morphology in multilayered CrN coating during indentation: Experiment and simulation, Mater. Des. 188 (2020).
[54] W.C. Oliver, G.M. Pharr, An improved technique for determining hardness and elastic modulus using load and displacement sensing indentation experiments, J. Mater. Res. 7 (1992) 1564–1583.
[55] G. Benecke, W. Wagermaier, C. Li, M. Schwartzkopf, G. Flucke, R. Hoerth, I. Zizak, M. Burghammer, E. Metwalli, P. Müller-Buschbaum, M. Trebbin, S. Förster, O. Paris, S.V. Roth, P. Fratzl, A customizable software for fast reduction and analysis of large X-ray scattering data sets: Applications of the new DPDAK package to small-angle X-ray scattering and grazing-incidence small-angle X-ray scattering, J. Appl. Crystallogr. 47 (2014) 1797–1803.
[56] J.C. Lagarias, J.A. Reeds, M.H. Wright, P.E. Wright, Convergence propoerties of the Nelder-Mead simpley method in low dimensions*, Siam. J. Optim. 9 (1998) 112–147.
[57] H. Möller, M. Gerhard, Elastische Anisotropie und röntgenographische Spannungsmessung, Verlag. Stahleisen (1939).
[58] C. Zener, Classical theory of the temperature dependence of magnetic anisotropy energy, Phys. Rev. 96 (1954) 1335–1337.
[59] A. Cornec, E. Lilleodden, Numerical analysis of micropillar compression behaviour and stress-strain curve estimation verified on glass fused silica, Mater. Today. Commun. 33 (2022).
[60] J. Keckes, R. Daniel, J. Todt, J. Zalesak, B. Sartory, S. Braun, J. Gluch, M. Rosenthal, M. Burghammer, C. Mitterer, S. Niese, A. Kubec, 30 nm X-ray focusing correlates oscillatory stress, texture and structural defect gradients across multilayered TiN-SiOx thin film, Acta. Mater. 144 (2018) 862–873.
[61] T. Gnäupel-Herold, ISODEC: Software for calculating diffraction elastic constants, J. Appl. Crystallogr. 45 (2012) 573–574.
[62] E. Kröner, Berechnung der elastischen Konstanten des Vielkristalls aus den Konstanten des Einkristalls, Z. Physik. 151 (1958) 504–518.
[63] T. Gnäupel-Herold, A.A. Creuziger, M. Iadicola, A model for calculating diffraction elastic constants, J. Appl. Crystallogr. 45 (2012) 197–206.
[64] H. Behnken, Mikrospannungen in vielkristallinen und heterogenen Werkstoffen, Shaker-Verlag (2003).
[65] A. Reuss, Berechnung der Fließgrenze von Mischkristallen auf Grund der Plastizitätsbedingung für Einkristalle, Z. Angew. Math. Mech. 9 (1929) 49–58.
[66] W. Voigt, Lehrbuch der Kristallphysik (mit Ausschluss der Kristalloptik), Teubner, B.G, 1910.
[67] J.D. Eshelby, The Determination of the Elastic Field of an Ellipsoidal Inclusion, Proc. R. Soc. Lond. A. 1226 (1957) 376–396.
[68] U. Welzel, J. Ligot, P. Lamparter, A.C. Vermeulen, E.J. Mittemeijer, Stress analysis of polycrystalline thin films and surface regions by X-ray diffraction, J. Appl. Crystallogr. 38 (2005) 1–29.
[69] G. Kresse, J. Furthmüller, Efficient iterative schemes for ab initio total-energy c alculations using a plane-wave basis set, Phys. Rev. B. 54 (1996) 11169–11186.
[70] G. Kresse, D. Joubert, From ultrasoft pseudopotentials to the projector augmented-wave method, Phys. Rev. B. 59 (1999) 1758–1775.
[71] J.P. Perdew, K. Burke, M. Ernzerhof, Generalized Gradient Approximation Made Simple, Phys. Rev. Lett. 77 (1996) 3865–3868.
[72] W. Kohn, L.J. Sham, PHYSICAL REVIEW Self-Consistent Equations Including Exchange and Correlation Effects, Phys. Rev. 140 (1965) A1133–A1138.
[73] S.-H. Wei, L.G. Ferreira, J.E. Bernard, A. Zunger, Electronic properties of random alloys: Special quasirandom structures, Phys. Rev. B. 42 (1990) 9622.
[74] D.G. Sangiovanni, F. Tasnádi, L.J.S. Johnson, M. Odén, I.A. Abrikosov, Strength, transformation toughening, and fracture dynamics of rocksalt-structure $Ti_{1-x}Al_xN$ ($0 \leq x \leq 0.75$) alloys, Phys. Rev. Mater. 4 (2020) 033605.
[75] M. Moakher, A.N. Norris, The closest elastic tensor of arbitrary symmetry to an elasticity tensor of lower symmetry, J. Elast. 85 (2006) 215–263.
[76] R. Hill, The Elastic Behaviour of a Crystalline Aggregate, Proc. Phys. Soc. A. 65 (1952) 349–354.
[77] J.F. Nye, Physical Properties of Crystals, Oxford University Press, 1985.
[78] S. Gates-Rector, T. Blanton, The Powder Diffraction File: a quality materials characterization database, Powder. Diffr. 34 (2019) 352–360.
[79] G. Abadias, E. Chason, J. Keckes, M. Sebastiani, G.B. Thompson, E. Barthel, G. L. Doll, C.E. Murray, C.H. Stoessel, L. Martinu, Review Article: Stress in thin films and coatings: Current status, challenges, and prospects, J. Vac. Sci. Technol. A. 36 (2018) 020801.
[80] J.O. Kim, J.D. Achenbach, P.B. Mirkarimi, M. Shinn, S.A. Barnett, Elastic constants of single-crystal transition-metal nitride films measured by line-focus acoustic microscopy, J. Appl. Phys. 72 (1992) 1805–1811.
[81] J. Almer, U. Lienert, R.L. Peng, C. Schlauer, M. Odén, Strain and texture analysis of coatings using high-energy x-rays, J. Appl. Phys. 94 (2003) 697–702.
[82] M. Zhang, J. He, Ab-initio calculation of elastic constants of TiN, Surf. Coat. Technol. 142–144 (2001) 125–131.
[83] L. Spieß, G. Teichert, R. Schwarzer, H. Behnken, Ch. Genzel, Moderne Röntgenbeugung, Vieweg+Teubner Verlag Wiesbaden, 2009.
[84] P.J. Withers, M. Preuss, A. Steuwer, J.W.L. Pang, Methods for obtaining the strain-free lattice parameter when using diffraction to determine residual stress, J. Appl. Crystallogr. 40 (2007) 891–904.
[85] R. Hahn, A. Tymoszuk, T. Wojcik, A. Kirnbauer, T. Kozák, J. Čapek, M. Sauer, A. Foelske, O. Hunold, P. Polcik, P.H. Mayrhofer, H. Riedl, Phase formation and mechanical properties of reactively and non-reactively sputtered Ti-B-N hard coatings, Surf. Coat. Technol. 420 (2021).